JEMS: A Deep Medium-band Imaging Survey in the Hubble Ultra Deep Field with JWST NIRCam and NIRISS

Christina C. Williams[1,2,23] , Sandro Tacchella[3,4] , Michael V. Maseda[5] , Brant E. Robertson[6] , Benjamin D. Johnson[7] ,
Chris J. Willott[8] , Daniel J. Eisenstein[7] , Christopher N. A. Willmer[2] , Zhiyuan Ji[2] , Kevin N. Hainline[2] ,
Jakob M. Helton[2] , Stacey Alberts[2] , Stefi Baum[9] , Rachana Bhatawdekar[10] , Kristan Boyett[11,12] , Andrew J. Bunker[13] ,
Stefano Carniani[14] , Stephane Charlot[15] , Jacopo Chevallard[13] , Emma Curtis-Lake[16] , Anna de Graaff[17] , Eiichi Egami[2] ,
Marijn Franx[18] , Nimisha Kumari[19] , Roberto Maiolino[3,4] , Erica J. Nelson[20] , Marcia J. Rieke[2] , Lester Sandles[3,4] ,
Irene Shivaei[2] , Charlotte Simmonds[3,4] , Renske Smit[21] , Katherine A. Suess[6,22] , Fengwu Sun[2] , Hannah Übler[3,4] , and
Joris Witstok[3,4]
[1] NSF's National Optical-Infrared Astronomy Research Laboratory, 950 N. Cherry Avenue, Tucson, AZ 85719, USA; christina.williams@noirlab.edu
[2] Steward Observatory, University of Arizona, 933 N. Cherry Avenue, Tucson, AZ 85721, USA
[3] Kavli Institute for Cosmology, University of Cambridge, Madingley Road, Cambridge, CB3 0HA, UK
[4] Cavendish Laboratory, University of Cambridge, 19 JJ Thomson Avenue, Cambridge, CB3 0HE, UK
[5] Department of Astronomy, University of Wisconsin-Madison, 475 N. Charter Street, Madison, WI 53706, USA
[6] Department of Astronomy and Astrophysics, University of California, Santa Cruz, 1156 High Street, Santa Cruz, CA 95064, USA
[7] Center for Astrophysics, Harvard & Smithsonian, 60 Garden Street, Cambridge, MA 02138, USA
[8] NRC Herzberg, 5071 West Saanich Road, Victoria, BC V9E 2E7, Canada
[9] Dept. of Physics & Astronomy, University of Manitoba, 30A Sifton Road, Winnipeg, MB R3T 2N2 Canada
[10] European Space Agency (ESA), European Space Astronomy Centre (ESAC), Camino Bajo del Castillo s/n, E-28692 Villanueva de la Cañada, Madrid, Spain
[11] School of Physics, University of Melbourne, Parkville 3010, VIC, Australia
[12] ARC Centre of Excellence for All Sky Astrophysics in 3 Dimensions (ASTRO 3D), Australia
[13] Department of Physics, University of Oxford, Denys Wilkinson Building, Keble Road, Oxford OX1 3RH, UK
[14] Scuola Normale Superiore, Piazza dei Cavalieri 7, I-56126 Pisa, Italy
[15] Sorbonne Université, CNRS, UMR 7095, Institut d'Astrophysique de Paris, 98 bis bd Arago, F-75014 Paris, France
[16] Centre for Astrophysics Research, Department of Physics, Astronomy and Mathematics, University of Hertfordshire, Hatfield AL10 9AB, UK
[17] Max-Planck-Institut für Astronomie, Königstuhl 17, D-69117, Heidelberg, Germany
[18] Leiden Observatory, Leiden University, P.O. Box 9513, NL-2300 AA Leiden, The Netherlands
[19] AURA for the European Space Agency, Space Telescope Science Institute, 3700 San Martin Drive, Baltimore, MD 21218, USA
[20] Department for Astrophysical and Planetary Science, University of Colorado, Boulder, CO 80309, USA
[21] Astrophysics Research Institute, Liverpool John Moores University, 146 Brownlow Hill, Liverpool L3 5RF, UK
[22] Kavli Institute for Particle Astrophysics and Cosmology and Department of Physics, Stanford University, Stanford, CA 94305, USA

Abstract

We present JWST Extragalactic Medium-band Survey, the first public medium-band imaging survey carried out using JWST/NIRCam and NIRISS. These observations use $\sim$2 and $\sim$4 μm medium-band filters (NIRCam F182M, F210M, F430M, F460M, F480M; and NIRISS F430M and F480M in parallel) over 15.6 arcmin^2 in the Hubble Ultra Deep Field (UDF), thereby building on the deepest multiwavelength public data sets available anywhere on the sky. We describe our science goals, survey design, NIRCam and NIRISS image reduction methods, and describe our first data release of the science-ready mosaics, which reach 5σ point-source limits (AB mag) of $\sim$29.3–29.4 in 2 μm filters and $\sim$28.2–28.7 at 4 μm. Our chosen filters create a JWST imaging survey in the UDF that enables novel analysis of a range of spectral features potentially across the redshift range of $0.3 < z < 20$, including Paschen-α, Hα+[N II], and [O III]+Hβ emission at high spatial resolution. We find that our JWST medium-band imaging efficiently identifies strong line emitters (medium-band colors >1 mag) across redshifts $1.5 < z < 9.3$, most prominently Hα+[N II] and [O III]+Hβ. We present our first data release including science-ready mosaics of each medium-band image available to the community, adding to the legacy value of past and future surveys in the UDF. This survey demonstrates the power of medium-band imaging with JWST, informing future extragalactic survey strategies using JWST observations.

Unified Astronomy Thesaurus concepts: Emission line galaxies (459); High-redshift galaxies (734); Redshift surveys (1378); Extragalactic astronomy (506)

1. Introduction

Optical and infrared extragalactic deep-field surveys have revealed that during the first few billion years after the Big Bang,

galaxies rapidly evolved under very different physical conditions than galaxies today. At fixed mass, early galaxies are smaller, have lower metal content, and contain stars that produce harder ionizing radiation fields, driving strong ionized gas emission lines in their interstellar medium (ISM; e.g., Stark 2016; Strom et al. 2017; Katz et al. 2023). The extreme physical conditions inside young galaxies at early times are now thought to be capable of reionizing the intergalactic medium (IGM; e.g., Bunker et al. 2010; Robertson et al. 2013; Atek et al. 2015; Maseda et al. 2020; Matthee et al. 2022). Meanwhile, recent studies using spectroscopy have demonstrated that massive quiescent galaxies begin to emerge

after only 1–2 billion years (Glazebrook et al. 2017; Schreiber et al. 2018; Forrest et al. 2020; Valentino et al. 2020; Nanayakkara et al. 2022). These are the mature relics of rapid, extreme growth toward the end of the Reionization Era (e.g., Marrone et al. 2018; Casey et al. 2019; Wang et al. 2019; Williams et al. 2019; Sun et al. 2021; Manning et al. 2022; Long et al. 2023). Even after the epoch of reionization completes, the majority of galaxies experience their most vigorous growth phases during the era of Cosmic Noon ($1 < z < 3$), forming new stars at unprecedentedly high rates across the Universe (e.g., Madau & Dickinson 2014).

A better understanding of the physical drivers of early galaxy evolution requires data that accurately capture spectral features, which provide more robust indicators of galaxy properties, overcoming the degeneracies between redshift, age, and dust reddening in spectral energy distributions (SEDs). The unknown contribution of emission lines to broadband fluxes has hampered high-redshift studies, and still impacts analysis using only JWST broadband photometry. While spectroscopic follow-up surveys have made important strides in characterizing spectral features for bright galaxies, major uncertainties remain for the fainter galaxies. An additional barrier to a complete picture of galaxy assembly is the incomplete knowledge about subkiloparsec spectroscopic signatures within distant galaxies. Obtaining these data (e.g., with integral field spectroscopy) is extremely expensive at high redshift, and remains limited to small samples of bright galaxies. Spatially resolved data from slitless spectroscopy or imaging with small bandwidths provide an efficient path forward by increasing efficiency and provide larger unbiased samples. However, slitless spectroscopy still typically has brighter detection limits than those possible using imaging (e.g., Brammer et al. 2012; Colbert et al. 2013; Skelton et al. 2014). Thus, imaging that finely samples galaxy SEDs at high spatial resolution has the power to identify the drivers of structural evolution across populations using statistical samples, identifying where star formation occurs at the time of observation, and where the stars have formed in the past on galaxy population scales.

An efficient path forward is to increase the sampling of SEDs by imaging with medium-band filters. Optical and near-infrared narrow- and medium-band surveys have demonstrated the power of increased spectral resolution to reconstruct galaxy properties out to wavelengths $\lambda \lesssim 2\,\mu$m (e.g., Wolf et al. 2004; Scoville et al. 2007; Moles et al. 2008; van Dokkum et al. 2009; Cardamone et al. 2010; Whitaker et al. 2011; Pérez-González et al. 2013; Straatman et al. 2016; Bonoli et al. 2021; Esdaile et al. 2021). In particular, such surveys have decreased photometric redshift uncertainties to 1%–2% by spanning the redshifted Balmer/4000 Å breaks for bright galaxies (to typical 5σ detection limits of <23–26 AB mag). By doing so, these surveys have provided insight into the evolution of galaxy types by breaking the degeneracy between age and dust among red galaxy types out to $z \sim 4$. Beyond this redshift, the bluest of strong rest-frame optical features, the Balmer/4000 Å break, leaves the ground-based observational window ($\lambda \lesssim 2\,\mu$m). Progress requires fainter detection limits and finer spectral sampling in key, unexplored wavelength ranges between 2 and 5 μm. As an additional preview of the power of medium bands at these wavelengths, the emission lines in early galaxies have been shown capable of boosting Spitzer/IRAC fluxes at $z > 4$ despite very broad bandpasses (see review in Bradač 2020, and references therein). These previous works motivate surveys using medium bands at longer wavelengths to better break the

degeneracies between continuum-break amplitude and line flux, and improve photometric redshifts.

Now that JWST has launched (Gardner et al. 2023), it is revealing enormous discovery space across cosmic time (see review by Robertson 2022). A unique feature of JWST among space telescopes is the suite of medium-band filters spanning 1–5 μm on board its near-infrared camera (NIRCam; Rieke et al. 2005, 2023), and its near-infrared imager and slitless spectrograph (NIRISS; Doyon et al. 2012; Willott et al. 2022), enabling improved spectral sampling that can both measure and spatially resolve individual spectral features such as emission lines and continuum breaks. This capability not only enables serious improvements to redshift measurements, but the unprecedented sensitivity of JWST also enables much smaller uncertainties in inferring fundamental parameters of galaxies, to much fainter magnitudes than previously possible across all redshifts. Simulations of legacy deep-field data have demonstrated the power of including one medium-band filter among the suite of broadband filters to recover intrinsic galaxy properties (Kemp et al. 2019; Kauffmann et al. 2020; Curtis-Lake et al. 2021; Roberts-Borsani et al. 2021; Tacchella et al. 2022). As such, many extragalactic surveys planned in JWST Cycle 1 include one to two medium bands to improve redshifts and SED measurements, including JADES (Eisenstein et al. 2023), CEERS (Bagley et al. 2023a), PRIMER (Dunlop et al. 2021), PANORAMIC (Williams et al. 2021), UNCOVER (Bezanson et al. 2022), PEARLS (Windhorst et al. 2023), or even full suites of medium-band filters (e.g., CANUCS; Willott et al. 2022).

This paper describes the JWST Extragalactic Medium-band Survey (JEMS), the first public imaging survey using more than two medium-band filters on board JWST at 2–5 μm. Our survey makes use of five medium bands at key wavelength ranges (2 and 4 μm) where increased sampling of the SED of high-redshift galaxies can break important degeneracies in galaxy properties (see Figure 1). Thus, these data will improve the power of JWST data to reveal the physical processes of galaxy evolution (e.g., Curtis-Lake et al. 2021), to faint limits below typical spectroscopic surveys even in the era of JWST (see Chevallard et al. 2019) and at high spatial resolution *for the first time*. In Section 2, we outline our survey strategy and the JEMS data. In Section 3, we describe the data reduction procedure for each JWST instrument we use: NIRCam and NIRISS. In Section 4, we characterize our image characteristics and describe our procedure for photometric measurements. We conclude in Section 5 with the science drivers that motivated the design, and a demonstration of the science potential enabled by this data.

2. Observations

2.1. Survey Design

The observations for our program (PID 1963, PIs C. Williams, S. Tacchella, M. Maseda) were conducted on 2022 October 12. Our observations include three separate footprints in the GOODS-South field (GOODS-S; Giavalisco et al. 2004). These include a single NIRCam pointing in the Ultra Deep Field (UDF; Beckwith et al. 2006, NIRCam detector centered at R.A. = 03:32:34, decl. = −27:48:08), composed of two individual footprints made by modules A and B. This pointing with an orient angle of 307°.228 aligns NIRCam module A with the coverage of the deepest MUSE
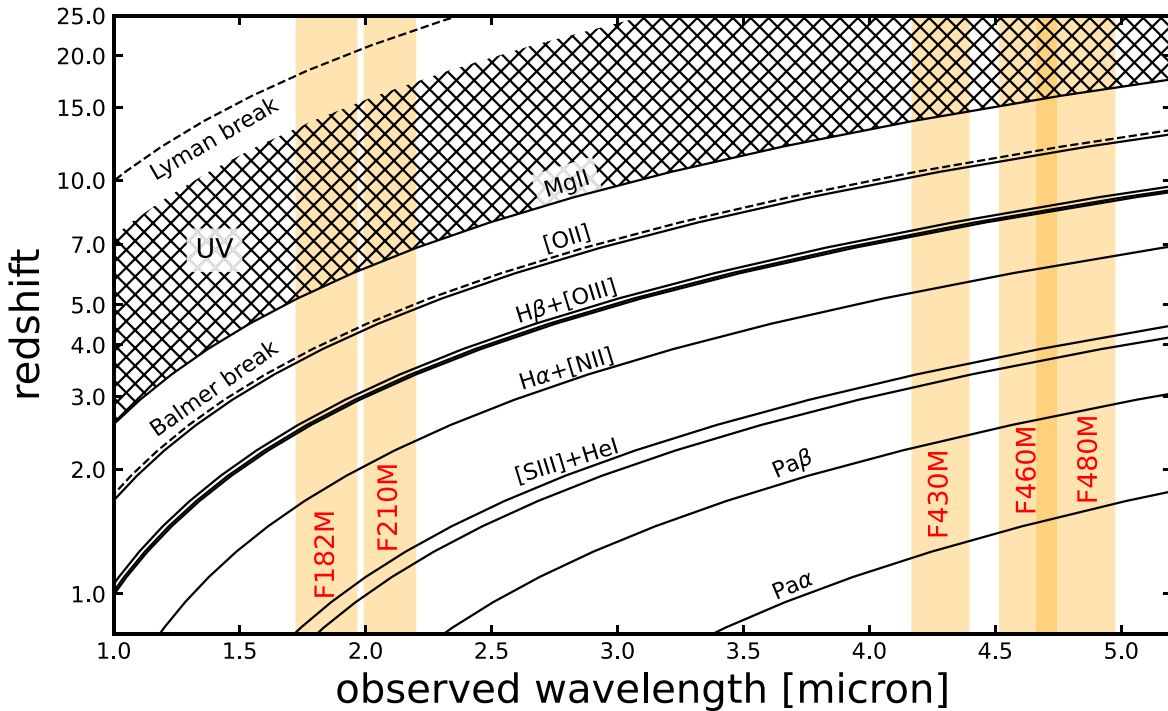
Figure 1. Key spectral features as a function of redshift in the five medium-band filters (F182M, F210M, F430M, F460M, and F480M). Indicated are the Lyman break and Balmer break as dashed lines, the UV continuum (1200–2800 Å) as hatched band, and the various emission lines probed by our data.

and Hubble Space Telescope (HST) pointings and covers the whole UDF (Illingworth et al. 2016; Bacon et al. 2023). The second NIRCam module B lies in the surrounding region covered by HST by both GOODS and CANDELS (Grogin et al. 2011), which also has some of the deepest MUSE and Atacama Large Millimeter/submillimeter Array deep-field coverage on the sky to date. The entire NIRCam footprint is covered by ancillary near-infrared imaging from 0.9 to 4.4 μm from the JADES survey (Eisenstein et al. 2023). The observations consist of a single visit with three filter pairs: F210M-F430M (13,915 s), F210M-F460M (13,915 s), and F182M-F480M (27,830 s). We employ the DEEP8 readout pattern for all exposures and/or dithers (12 in total for F430M and F460M; 24 for F182M, F210M, and F480M) with six groups per integration and one integration per exposure.

A third footprint comes from performing a coordinated parallel with NIRISS imaging (using F430M and F480M filters), which increases the survey area at 4.3 and 4.8 μm wavelengths by 50%. The NIRISS footprint has a pointing center at 03:32:34, −27:54:01. We use the NIS readout pattern with 26 groups per integration, and one integration per exposure, with total integration time of 28,087 s for the F430M and F480M filters each. The NIRISS pointing sits inside CANDELS, and will have ∼50% coverage by the JADES near-infrared imaging by the end of 2023. The location of our imaging footprints within the GOODS-S field is shown in Figure 2, and we show a zoomed-in color composite of each footprint with a few example emission-line sources in Figure 3. Our total on sky area covered by both NIRCam and NIRISS is ∼15.6 arcmin².

The dithering pattern is fixed to INTRAMODULEBOX with four primary dither positions and a 3-POINT-MEDIUM-WITH-NIRISS for the subpixel dither type. We choose the INTRAMODULEBOX pattern since it is more compact than INTRAMODULE or INTRAMODULEX, thereby yielding

more area at full depth. The science exposure time is 15.47 hr, and the total charged time is 20.42 hr. Details of the observations using both instruments are listed in Table 1.

Our exposure times are motivated by probing the Hα emission in $z = 5.4$–6.6 galaxies, both on integrated and spatially resolved scales. We aimed to obtain a point-source line flux of 1–2×10^{-18} erg s^{-1} cm^{-2}, corresponding to a star formation rate (SFR) of $\sim 1\, M_\odot$ yr^{-1}, which probes a major part of the galaxy population at this epoch (see Section 5.3). In addition, we want to probe an Hα surface brightness of 4×10^{-18} erg s^{-1} cm^{-2} arcsec^{-2}, which enables a comparison of azimuthally averaged Hα profiles to the typical Lyα profiles out to the typical distance scales probed by MUSE (Wisotzki et al. 2018).

Further, our medium-band survey with JWST was motivated as an important complement to ongoing spectroscopic surveys in the UDF, including with grism (e.g., FRESCO; Oesch et al. 2023; NGDEEP; Bagley et al. 2023b) and the NIRSpec multiobject spectrograph (e.g., JADES; Eisenstein et al. 2023). Medium-band imaging has more sensitive detection limits compared to grism spectroscopy per unit exposure time, because the grism reduces the throughput, covers a smaller effective area with both imaging and spectra per pointing, and, for some galaxies with high velocity spread, resolves the line flux over more pixels. A major technical challenge for grism observations involves overlapping source contamination along with blurring of the galaxy structure in the dispersion direction. Medium-band imaging is thus an incredibly powerful complementary data set to help disentangle sources and reconstruct spatially resolved emission lines. Further, the medium-band photometry can constrain the slit losses in NIRSpec emission-line measurements, a major uncertainty in particular for the multishutter array, whose fixed grid of slitlets means galaxies are not always centered in their slits (Ferruit et al. 2022).
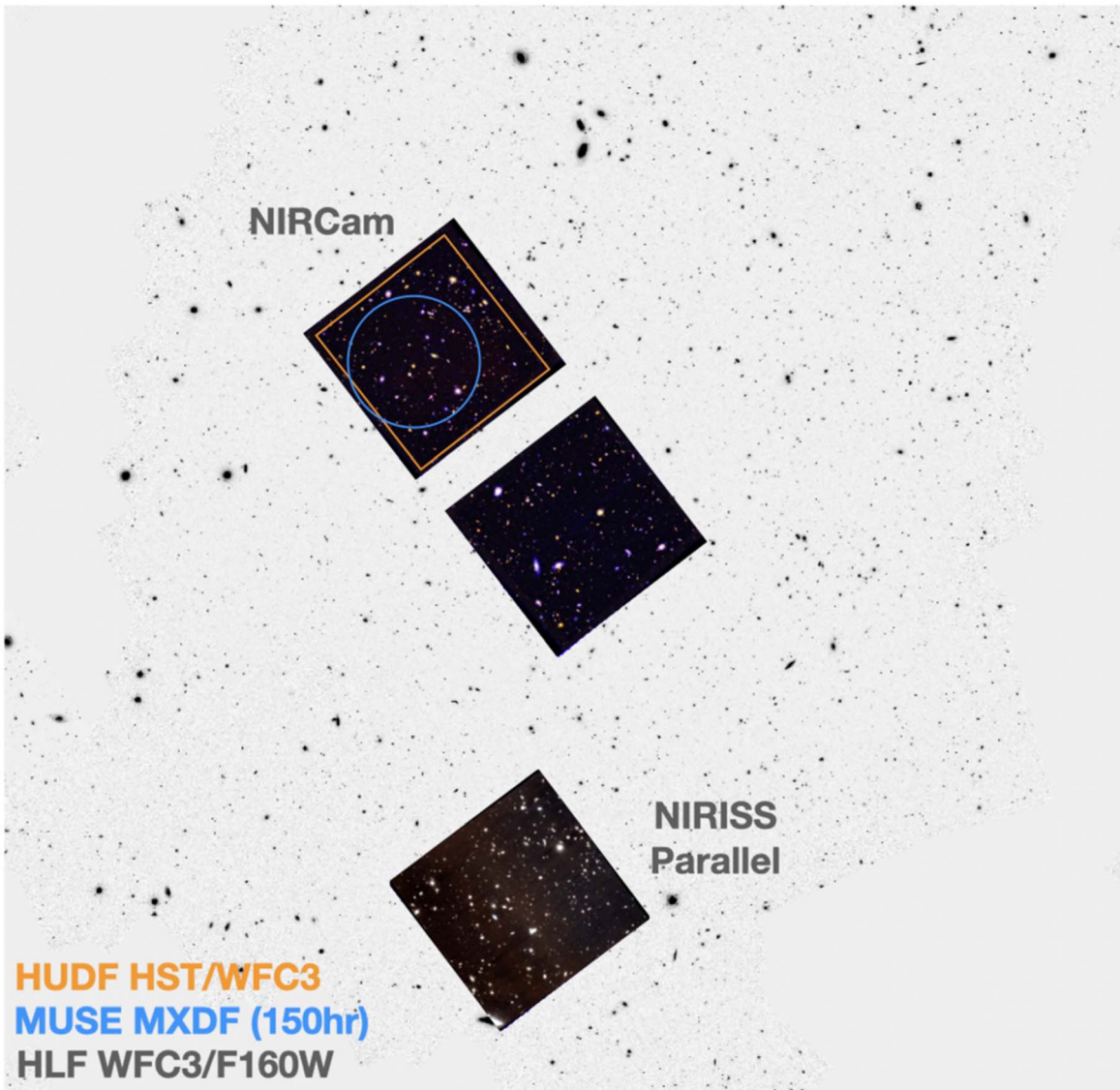
Figure 2. Layout of our NIRCam and NIRISS pointings in the GOODS-S field (HLF WFC3/F160W imaging, inverted gray scale, corrected to the Gaia astrometry). Colored regions indicate the footprint of various legacy data in the HUDF, covered by our NIRCam module A: HUDF WFC3/IR (orange), and MUSE MXDF (blue). RGB color composites of our JWST footprints are blue as F430M, green as F460M, red as F480M for NIRCam; and blue as F430M, green as F430M+F480M, red as F480M for NIRISS.

2.2. Ancillary Data

To characterize the sources detected in our survey later in this work (see Section 5.2), we combine our imaging with existing ancillary data, which is the deepest among all legacy fields in the sky. In particular, we make use of the Hubble Legacy Field (HLF; Illingworth et al. 2016; Whitaker et al. 2019, and references therein) imaging in GOODS-S from HST, which represents the deepest composite imaging including nine filters between 0.4 and 1.6 μm wavelength (F435W, F606W, F775W, F814W, F850LP, F105W, F125W, F140W, F160W). We document our astrometric alignment procedure of these data with our JWST imaging in the Appendix. We also include photometry measured from the JADES NIRCam imaging obtained as of 2022 November, which covers our NIRCam footprint (JADES data and processing methodology are presented in detail in Eisenstein et al. 2023; Rieke & the JADES Collaboration 2023). The JADES imaging in our footprint covers nine filters across 0.9–4.4 μm wavelengths (F090W, F115W, F150W, F200W, F277W, F335M, F356W, F410M, F444W).

The HUDF is also home to extensive public and archival spectroscopy. We make use of a spectroscopic compilation of galaxies from the GOODS-S field as compiled in Kodra et al. (2023), references therein (their Table 6; N. Hathi 2023, private communication). We also include (and override the others in case of overlap) with the latest MUSE data release (Bacon et al. 2023) and a preliminary list of spectroscopic identifications from FRESCO (Oesch et al. 2023), both of which target redshifts where our medium-band imaging is most sensitive to line emitters ($z > 3$). We only use redshifts that have been identified as secure or reliable and exclude uncertain or poor quality solutions.

3. Data Reduction

3.1. NIRCam Image Reduction

Our NIRCam image processing follows the methodology developed for the JADES survey. Full details of the JADES
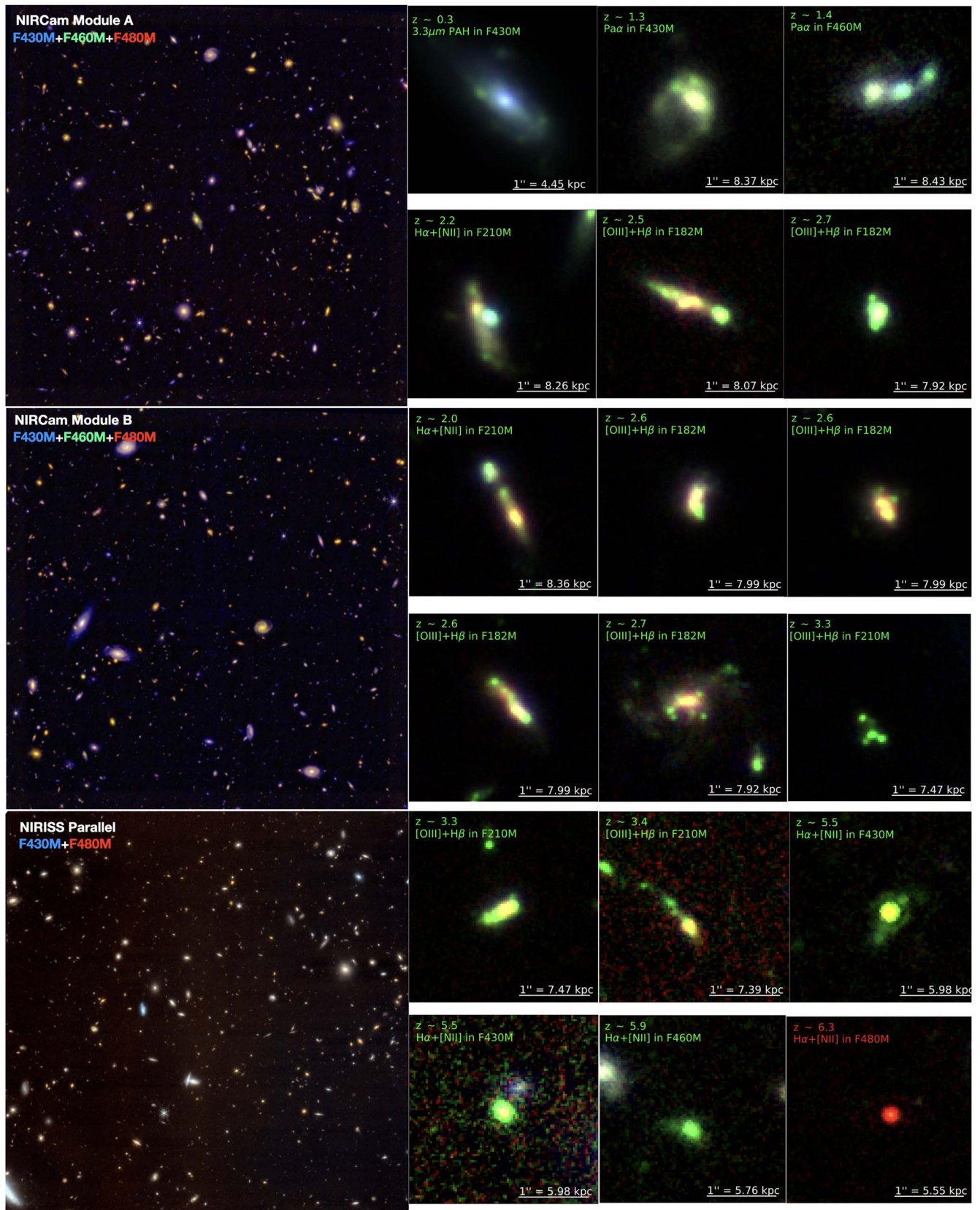
Figure 3. Left: color composite images (for NIRCam, blue is F430M, green is F460M, red is F480M; and for NIRISS, blue is F430M, and red is F480M) for our three JWST pointings (as in Figure 2). Right: color composite cutouts of spectroscopically confirmed galaxies at various redshifts whose colors trace emission-line features (in order of increasing redshift). Blue, WFC3/160W; red, F480M; green, JWST filter where the corresponding emission line is. For F480M line emitters, we use the F460M as green in the RGB. Note different color coding between mosaics and cutouts.

imaging data reduction will be presented in S. Tacchella et al. (2023, in preparation; see also Rieke & the JADES Collaboration 2023), including performance tests. We summarize here the main steps for completeness. We use version 1.9.6 of the Space Telescope Science Institute (STScI) JWST calibration pipeline. We use context map Calibration Reference Data System (CRDS) reference file `jwst_1084.pmap`. Importantly, this context map includes updates from `jwst_0995.pmap`, which has the most recent absolute flux calibration for NIRCam detectors using our chosen medium bands from observations collected by calibration programs PID 1536, 1537, and 1538 (PI: K. Gordon; Boyer et al. 2022; Gordon et al. 2022).

We run stage 1 of the pipeline with its default parameters. This stage performs detector-level corrections and produces count-rate images. We correct snowballs in the images caused by charge deposition following cosmic ray hits. We adopt the default values for stage 2 of the JWST pipeline, which performs the flat-fielding and applies the flux calibration. Importantly, we replace the STScI flats with supersky flats for the JADES and JEMS LW bands.

Following stage 2, we perform several custom corrections in order to account for several features in the NIRCam images (e.g., Rigby et al. 2023). In particular, we remove the $1/f$ noise by fitting for a parametric model along rows and columns on the source-masked images.[24] Following this, we subtract a smooth background image that we construct with the `photutils` (Bradley et al. 2022) Background2D class. For the short-wavelength channel images (in particular, the NIRCam detectors A3, A4, B3, and B4 for the filters F182M and F210M), we simultaneously subtract scattered light artifacts (i.e., "wisps," Rigby et al. 2023). We have constructed wisp templates by stacking all images from our JADES (PID 1180 and 1181) program and several other programs (PIDs 1063, 1345, 1837, 2738) after reducing them following the same approach as outlined above. The templates are rescaled to account for the variable brightness of the wisp features and then subtracted from the images.

Before combining the individual exposures into a mosaic, we perform astrometric relative and absolute corrections with a custom version of JWST TweakReg. We group individual detector images by exposure number and then match sources to a reference catalog constructed from HST F160W mosaics in the GOODS-S field with astrometry tied to Gaia Early Data Release 3 (Gaia Collaboration et al. 2016, 2018; G. Brammer et al. 2023, in preparation). These matches are used to calculate a tangent plane shift and rotation for each exposure. We then group the images by visit and band and apply the median shift and rotation for each group to all images in that group. At the time of writing, the flight versions of the distortion modeling for the medium bands we used were not yet included in the CRDS. We override the default distortion model reference for the $2\,\mu m$ medium-band filters to use the distortion model for the nearest broadband filters (F200W for F182M and F210M, and F444W for F430M, F460M, F480M). We then run stage 3 of the JWST pipeline, combining all exposures of a given filter. We choose a pixel scale of $0\rlap{.}{''}03\,\mathrm{pixel}^{-1}$ for both SW and LW channel images and choose the drizzle parameters (Fruchter & Hook 2002) of `pixfrac = 1` and 0.7 for the 2 and $4\,\mu m$ images, respectively.

---

[24] https://github.com/chriswillott/jwst

Filter	Integration Time (s)	5σ Sensitivity (AB mag)	Survey Area
NIRCam			10.1 arcmin^2
F182M	27,830	29.4	
F210M	27,830	29.3	
F430M	13,915	28.5	
F460M	13,915	28.2	
F480M	27,830	28.6	
NIRISS			5.5 arcmin^2
F430M	27,057	28.7	
F480M	27,057	28.5	

Note. Point-source sensitivity is measured using $0\rlap{.}{''}3$ diameter apertures, aperture corrected to total magnitudes as described in Section 4.2.

3.2. NIRISS Image Reduction

The NIRISS images were processed with version 1.8.4 of the JWST calibration pipeline with CRDS context `jwst_1019.pmap`. Stage 1 of the pipeline included the optional snowball correction in the jump step. Two custom steps were run during stage 1: removal of random DC offsets along the detector columns using the NIRISS columnjump code (see footnote 24) and flagging groups in pixels that are affected by persistence from the previous exposure. Stage 2 processing incorporated a $1/f$ noise correction on each flat-fielded rate file utilizing background subtraction and source masking to isolate the noise stripes from spatially varying background or sources. A constant background model incorporating the NIRISS light saber scattered light feature (Doyon et al. 2023) was subtracted from each F430M exposure. The F480M data did not show a significant light saber feature. The 24 NIRISS exposures in each filter were then mosaicked with stage 3 of the pipeline utilizing an absolute astrometry reference catalog from JADES NIRCam imaging that overlaps almost half of the field (which are also astrometrically calibrated based on the same method described in Section 3.1). Finally, a low-level fitted 2D background model was subtracted from the mosaicked images. The NIRISS mosaic is drizzled onto a 30 mas pixel scale.

4. Image Properties

In this section, we characterize the properties of our final image mosaics including achieved depth, and number of sources detected in each band. To characterize our JEMS data, we perform source detection and measure photometry in our imaging following the same methodology as the photometric catalog released by the JADES team (Rieke & the JADES Collaboration 2023).

4.1. Source Detection

Detection images are constructed based on the inverse variance weighting of JWST/NIRCam using SCI flux extension and ERR flux error extension (which includes sky, read, and poisson noise added in quadrature) using astropy (Astropy Collaboration et al. 2022). In brief, detection images are based on a stack of the long-wave filters in the JEMS-overlapping JADES imaging (F277W, F335M, F356W, F410M, F444W; Eisenstein et al. 2023). Detections are identified using

photutils (Bradley et al. 2022) with an optimized set of algorithms that perform source deblending, remove spurious sources and persistence artifacts, and reblend shredded parent objects. The methods are outlined in full detail in Rieke & the JADES Collaboration (2023; their Section 4) and B. Robertson et al. (2023, in preparation).

In addition to using sources detected based on the JADES data release methods, we additionally create detection images for each of the five medium-band filters individually to ensure that we identify strong line emitters that may be missed by a longwavelength stack. For this purpose, we follow a simpler procedure and identify detections as contiguous regions in the detection image with a minimum area of 10 pixels that contain signal-to-noise ratio $(S/N) > 3$ using photutils (Bradley et al. 2022). We then apply a standard deblending algorithm to the detection image with parameters nlevels = 32, and contrast = 0.001 (Bertin & Arnouts 1996). While we find that the overwhelming majority of nonartifact objects from the individual band detection are identified in the JADES detection, we note a small number of likely real, but faint additional emission-line sources that are retrieved by our detection. We find that these are excluded from JADES because they are blended with bright low-redshift neighbors, and thus, this is likely a consequence of the procedure for reblending shredded parents. Since the detection and deblending algorithm choices are a trade-off that enables cleaner artifact rejection and source identification, we determine that these features outweigh the benefit of detecting a handful of faint emission-line sources. For simplicity, we therefore opt to add the forced photometry for these few missed sources to our analysis of the JADES catalog in Section 4.2 and analysis in Section 5.

4.2. Photometry

To characterize our survey performance, we use photutils to perform forced photometry in fixed apertures of diameter $0\rlap{.}''3$ at the locations of our stacked detections. To measure photometric uncertainty in our forced apertures, we use 100,000 random apertures in sourceless regions identified using our source detection mask and measure the flux in the apertures, enabling us to include the additional noise source from pixel covariance in our uncertainty. We estimate aperture corrections for flux lost from the fixed apertures by interpolating encircled energy curves based on model point-spread functions (mPSFs). These mPSFs were constructed using webbPSF (v1.1.1 Perrin et al. 2014) while taking into account the source location on the detector and data reduction methods as outlined in Ji et al. (2023). These are consistent with the overlapping JADES data products presented in Rieke & the JADES Collaboration (2023).

With these criteria, we identify 7801 sources with significant flux at $>5\sigma$ in at least one JEMS filter. Using detections in individual filters, we find 7333, 6682, 4328, 3484, 4079 sources (for F182M, F210M, F430M, F460M, and F480M, respectively). These include 11 sources that are detected in only 1 filter (5σ), representing candidates for strong emission-line galaxies below the JEMS continuum detection limit.

4.3. Image Results

We measure the limiting 5σ depth of our images using the measured photometry of sources in $0\rlap{.}''3$ diameter apertures and the uncertainty measured in the random apertures described in the last section, which includes the impact of increased noise due to pixel covariance introduced by our mosaicing methodology. Thus, our final mosaics are slightly shallower than the predictions from the Exposure Time Calculator (which excludes the uncertainty introduced by pixel covariance) ranging from $\sim$0.1–0.15 and $\sim$0.05–0.1 mag in the NIRCam shortwave and longwave filters (respectively), and $\lesssim$0.05 with NIRISS. The 5σ magnitude limits (aperture corrected) in fixed apertures of $0\rlap{.}''3$ diameter in our 5 filters are presented in Table 1.

5. Science

In this section, we present a view of the science potential of our medium-band imaging. We start by outlining the science drivers that motivated our survey design, in order of lookback time. We then present empirical findings for the galaxies for which we can measure emission-line properties across redshifts, and outline our data's sensitivity to emission-line properties based on mock data.

5.1. Science Objectives

The new parameter space of spectral features observed at $\sim$2 and $\sim$4 μm wavelengths enables a wealth of new science across cosmic time. Figure 1 shows the observed wavelength of the major spectral features in galaxies for different redshifts, and where they cross into the medium bands in our survey. New spectroscopic tracers are probed at nearly all redshifts from $0.3 < z < 20$. We structure the survey to allow exploration of the following science drivers.

5.1.1. Star Formation Activity in Galaxies during and after Cosmic Noon (z < 2.8)

One of the fundamental properties of galaxies is their SFR. Despite significant evolution in galaxy properties over cosmic time, SFR measurements are still based on locally calibrated diagnostics using nearby galaxies (Kennicutt & Evans 2012). These efforts have resulted in the *industry standard* SFR indicator based on UV+IR, which is efficient for extragalactic surveys out to $z \sim 2$. However, traditional *gold-standard* tracers that are least sensitive to dust attenuation have been inaccessible outside of the local Universe until JWST. Measuring the instantaneous SFR from infrared hydrogen recombination lines (e.g., Paschen-α) in both integrated and spatially resolved manner is a major step forward in our understanding of galaxy assembly.

Our 4 μm imaging probes 3.3 μm polycyclic aromatic hydrocarbon (PAH) emission at $z \lesssim 1$ (one of the least-explored PAH bands beyond the local Universe), Paschen lines Pa$\alpha\lambda$18750 and Pa$\beta\lambda$12820 at $z \sim 1.2$–2.8, enabling less attenuation-affected SFR measurements for lines that have historically been only accessible at $z < 0.3$ (e.g., Pasha et al. 2020; Giménez-Arteaga et al. 2022). These less attenuation-affected SFR measurements have until now been only possible for relatively extreme sources at low redshift (Calabrò et al. 2018; Cleri et al. 2022) or rare highly magnified cases that are not necessarily representative of the full galaxy populations (Papovich et al. 2009; Rujopakarn et al. 2012). While these lines are fainter than those from the Balmer series (even with no dust, Paα/Hα = 0.33, and Paβ/Hα = 0.16 for case B recombination), with the high sensitivity of JWST/NIRCam

and NIRISS, these measurements are in fact possible with medium-band photometry (see results presented in Section 5.2). Figure 4 demonstrates an F460M flux excess due to Paα emission in the SED of a mock star-forming galaxy at $z \sim 1.5$ from the JADES Extragalactic Ultradeep Artificial Realization (JAGUAR) mock catalog (Williams et al. 2018), whose SEDs are created using BEAGLE (Chevallard & Charlot 2016). In principle, for galaxies that exhibit strong lines that boost colors with high enough S/N, spatially resolved analyses can provide insight into how galaxies assemble their stellar mass (see Figure 3; Rujopakarn et al. 2023; S. Alberts et al. 2023, in preparation), building on previous studies with expensive integral field unit observations at the Very Large Telescope (e.g., Tacchella et al. 2015; Förster Schreiber et al. 2018) or HST grism (e.g., Nelson et al. 2016; Matharu et al. 2021).

5.1.2. Pre–Cosmic Noon ($2.5 \lesssim$ z < 5)

Prior to JWST, the ground-based observational limit at $\lambda \lesssim 2.5\,\mu m$, and the low spatial and photometric resolution of Spitzer/IRAC, imposed technical challenges to understanding galaxy evolution above $z > 3$. In particular, as the rest-frame optical diagnostics are redshifted beyond the high-resolution HST and deep ground-based K band into broad IRAC bands, degeneracies are created between rest-frame optical emission-line flux and continuum-break amplitude. These are the primary spectroscopic signatures that are leveraged for modeling the stellar populations in distant galaxies.

Our $2\,\mu m$ imaging traces the Balmer/4000 Å break at $3.3 < z < 4.5$, which is now thought to be an important era when massive galaxies reach their maturity. The increased spectral sampling enables better constrained measurements of stellar age due to more accurate tracing of the 4000 Å/Balmer break diagnostic at this key redshift range (see bottom panel of Figure 4). Ground-based limits made this only achievable for the most massive red galaxies (e.g., Esdaile et al. 2021), and JWST opens the window to explore quiescence among lower mass galaxies (e.g., Santini et al. 2022; Marchesini et al. 2023). We thus expect that medium-band imaging at $2\,\mu m$ will be crucial to identifying the epoch of the emergence of massive quiescent galaxies and reconstructing their star formation histories. The unprecedented spatial resolution will enable spatially resolved color gradients of "dead" galaxies that trace age and metallicity gradients, measurements previously relegated to distant objects sheared by lensing (Akhshik et al. 2020, 2023). These empirical measurements provide powerful tests of the process that drives their rapid formation when compared to cosmological simulations (e.g., Wellons et al. 2015; Tacchella et al. 2016; Nelson et al. 2021).

Among the most prominent features at this redshift range as seen in our $2\,\mu m$ data are the [O III]+Hβ emission lines visible at $2.4 < z < 3.5$ (see, e.g., top panel of Figure 5). This new redshift coverage of [O III]+Hβ now enables continuous characterization of the [O III]+Hβ evolution between the reionization era and the analogs at $z \sim 2$–3 that are typically used to infer broader conclusions about reionization physics (e.g., Nakajima et al. 2016; Fletcher et al. 2019; Barrow et al. 2020; Tang et al. 2021; Boyett et al. 2022), thus tracking the abundance of strong line emitters and their equivalent width (EW) distribution among galaxy populations. Additionally, combined with the high resolution of NIRCam at $2\,\mu m$, a new window is opened into the spatial distribution of star formation

and ionized gas within galaxies during a critical assembly period (Ji et al. 2023).

We also note the potential discovery space of new diagnostics in this redshift range. As shown in Figure 5 (third panel), the $4\,\mu m$ medium bands are expected to show strong color fluctuations with redshift due to the entrance and exit of [S III]λ9069, 9532+He I λ10830 between $2.8 < z < 4.2$ based on the JAGUAR mock catalog (Williams et al. 2018). These are not standard strong line diagnostics, but they are strong enough to also be visible at Cosmic Noon in the 3D HST grism survey (Momcheva et al. 2016). While these features will undoubtedly improve photometric redshifts and the modeling of stellar populations in this redshift range, new science is possible through measuring their line fluxes via photometric excesses (e.g., Mingozzi et al. 2020).

5.1.3. End of Reionization ($5.4 <$ z < 6.6)

Our data can ascertain if the flux excesses observed with Spitzer are due to Balmer breaks or due to contamination from strong rest-frame optical emission lines (e.g., Hα EW > 500 Å; Eyles et al. 2005, 2007; Shim et al. 2011; Stark et al. 2013; de Barros et al. 2014; Smit et al. 2015, 2016; Rasappu et al. 2016; Hatsukade et al. 2018; Faisst et al. 2019; Lam et al. 2019; Stefanon et al. 2022; Endsley et al. 2023; Sun et al. 2023). Strong lines are reflective of bursty galaxy growth, compact stellar distributions, and lower metallicity stars with harder ionizing radiation fields. Their properties are critical to understanding the process of Reionization since star-forming galaxies are favored to drive it; though, it is still debated which galaxies (bright versus faint) dominate (Bunker et al. 2004; Robertson et al. 2013; Bouwens et al. 2015; Finkelstein et al. 2019; Naidu et al. 2020). We still lack the necessary accounting of the production of ionizing photons from reionization era galaxies, and how they escape through the ISM and circumgalactic medium (CGM). Importantly, hydrogen-ionizing radiation will never be directly measured in the epoch of reionization (with mean redshift $z \sim 7$–8, ending by $z \sim 5$–6; e.g., Keating et al. 2020; Planck Collaboration et al. 2020). This is due to the opacity of the intervening neutral IGM (e.g., Inoue et al. 2014; McGreer et al. 2015), preventing an accurate measurement of the intrinsic ionizing photon production. The amount of dust attenuation and its geometry also remains significantly uncertain during these early phases of galaxy growth (e.g., Bowler et al. 2018, 2022).

Our three $4\,\mu m$ filters cover Hα+[N II] at $5.4 < z < 6.6$ (the tail end of reionization epoch), simultaneously with improved sampling of the rest-frame UV continuum shape with the $2\,\mu m$ filters. The imaging thus provides critical constraints on the SFRs, stellar masses, intrinsic ionizing photon production, and dust geometry within galaxies at high spatial resolution. Rest-frame optical emission-line maps will create a wealth of diagnostics to enable a detailed picture of reionization era galaxies: the properties of the massive stars that ionize gas, where ionizing radiation initiates in the galaxy, and in combination with ancillary data, how Lyα radiation propagates to the CGM and IGM (e.g., Ning et al. 2023; Simmonds et al. 2023).

5.1.4. Epoch of Reionization ($7.3 <$ z < 9.3)

Spitzer/IRAC photometric excesses have been observed, consistent with contamination from strong [O III]+Hβ emission
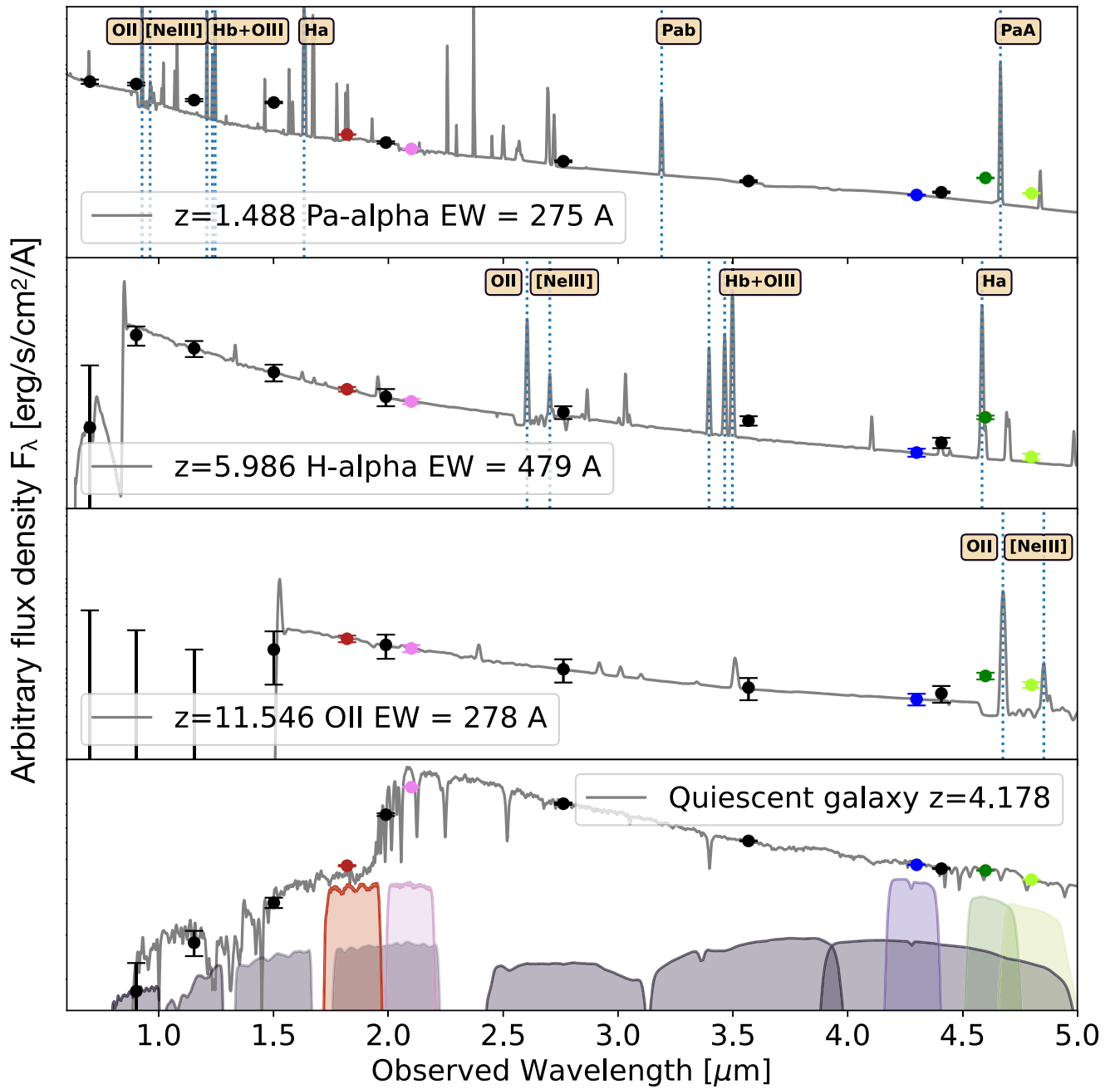
Figure 4. Example mock SEDs from JAGUAR (Williams et al. 2018) demonstrating the power of our medium-band imaging (colored transmission curves and photometric points) to measure spectral features, compared to NIRCam broadband filters from 0.9 to 5 μm (gray transmission curves and black points). SEDs are normalized at F277W (relative flux units). Top two panels include star-forming galaxies with key redshifts and spectral features: Paschen-α at $z \sim 1.4$, and Hα at $z \sim 6$ (both seen with the emission line in F460M). Third panel shows a $z \sim 11.5$ galaxy with O II flux boosting F460M. Bottom panel shows a quiescent galaxy at $z \sim 4.1$, where it is clear that our medium-band data robustly trace the balmer/4000 Å break spectral region compared to broad bands, thus improving age and mass measurements.

from redshifts $z \sim 4$–8 (e.g., Labbé et al. 2013; Smit et al. 2014, 2015; Faisst et al. 2016; De Barros et al. 2019; Endsley et al. 2021). Above $z > 7.3$, our 4 μm imaging yields a direct measurement of [O III]+Hβ at $z = 7.6$–9.3, and the combination of the three filters enables a deconstruction of any flux from the Balmer break, probing earlier eras of star formation (e.g., Laporte et al. 2023). This extends the accounting of ionizing photons and stellar populations deeper into the epoch of reionization, as strong [O III]+Hβ lines are signposts for ionizing sources (e.g., Endsley

et al. 2021), while additionally providing inferences on the mass and redshift dependence of ionizing photon production as well as robust measurements of the mass function (otherwise contaminated by lines). The presence of emission lines probed by our medium-band photometry additionally can provide better redshift confirmation of Lyman-break dropout samples identified with HST (e.g., Bunker et al. 2010; Wilkins et al. 2011; Lorenzoni et al. 2013; Bouwens et al. 2015, 2023; Finkelstein et al. 2015; Hainline et al. 2023).
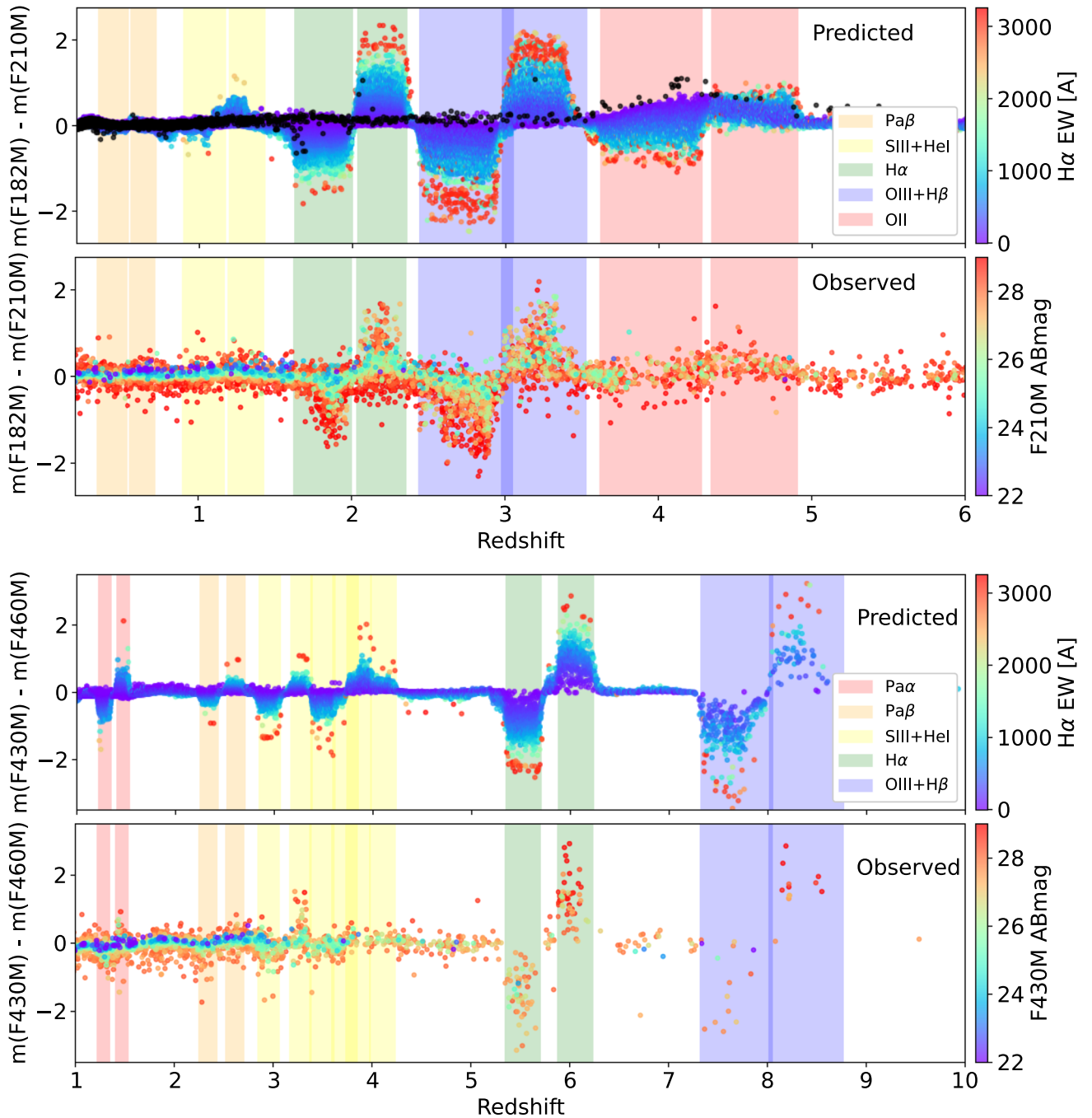
Figure 5. SED shapes and strong emission lines are identifiable by extreme 2 and 4 μm medium-band colors (e.g., F182M−F210M, top two panels; and F430M −F460M, bottom two panels). In the first and third panels, points represent predicted distributions from mock star-forming galaxies (Williams et al. 2018) detected in either filter at >7σ (flux limits in Table 2) color coded by their Hα rest-frame equivalent width (black points indicate quiescent galaxies). In the second and fourth panels, points are observed galaxies in our data, color-coded by their F430M apparent magnitude. In all panels, shaded bands indicate the emission feature boosting the flux at a given redshift. 2 μm distributions show more sources than 4 μm owing to the deeper detection limits.

5.1.5. Cosmic Dawn (9.3 < z < 20)

Limited samples of candidate galaxies with redshifts during Cosmic Dawn are known, with JWST now identifying the photometric candidates beyond the redshift limit of HST+Spitzer ($z \gtrsim 11$; Naidu et al. 2022; Bradley et al. 2023; Harikane et al. 2023; Adams et al. 2023; Atek et al. 2023a, 2023b; Donnan et al. 2023a; Finkelstein et al. 2023; Hainline et al. 2023). Once [O III]+Hβ redshifts outside of our 4 μm medium-band window,

our data provide access to novel spectral diagnostics for photometric data at these distant redshifts. These include the [O II]$\lambda\lambda$3727 line to $z \sim 10.2$–12.4, whose typical line strengths are currently unknown at such redshifts (e.g., third panel of Figure 4). Further, our data enable the potential for detecting breaks at the Balmer limit (rest-frame wavelength λ3650, probed by our data in the redshift range $z \sim 10.4$–12.6; see, e.g., Bouwens et al. 2023; Curtis-Lake et al. 2023; Donnan et al. 2023b;

Robertson et al. 2023), thus yielding the potential to reconstruct even yet earlier epochs of star formation (if it occurs, see, e.g., Labbe et al. 2023; Tacchella et al. 2023; Whitler et al. 2023). Between the sets of 2 and 4 μm filters, UV continuum colors are measurable to $z \sim 9$–23. Further, we note the potential for refined dropout selection with narrower redshift selection function at $z \gtrsim 14$ with the 2 μm filters.

5.2. Empirical Emission-line Constraints Using Medium-band Imaging

In this section, we characterize the galaxy population for which our deep imaging can provide new physical insight through refined SED sampling at unprecedented wavelength ranges (2–4 μm). We focus specifically on our NIRCam photometry, which has the best ancillary data for assessing performance, given its location in the HUDF with the deepest HST legacy imaging, existing imaging from the JADES survey, and the largest sample of spectroscopy at the relevant redshifts (Section 2.2).

To demonstrate the impact of spectral features (in particular, emission lines) on the medium-band colors, we plot the 2 μm colors (F182M − F210M) and one set of 4 μm colors (F430M − F460M) as a function of redshift in Figure 5. In the first and third panels, we show simulated color evolution with redshift using JAGUAR (Williams et al. 2018). This figure demonstrates that colors can reach more than 2 mag difference depending on the intrinsic emission-line properties of the galaxies (e.g., in the figure, we color the points by their intrinsic Hα equivalent width). This is by design much stronger than color evolution using JWST broadband filters (colors of order $\sim$0.5 mag as predicted by cosmological simulations, e.g., Wilkins et al. 2022). We also highlight the redshift ranges where major emission-line features enter and exit the filter bandpasses as colored bands. The number of galaxies at higher redshifts starts to decrease (e.g., in particular, at $z > 7$, as can be seen in the 4 μm colors in panel (3)). Therefore, in order to highlight the features of the distributions at high redshift, we maximize the number of galaxies in the distribution by plotting all JAGUAR sources down to stellar mass $>10^6$ $M_\odot$, and over 10 JAGUAR realizations ($\sim$1200 arcmin^2). While this mock area is significantly larger than that from our imaging survey, it is useful as a demonstration of how the medium-band colors scale with emission-line equivalent width. Additionally, we plot the 2 μm medium-band colors of quiescent JAGUAR galaxies (black points) to demonstrate the capability of characterizing emission lines and the movement of the 4000 Å break into and out of the filters above $z > 3$.

In the second and fourth panels, we show for comparison the colors versus redshift for real galaxies detected in at least one filter with S/N > 7 in our medium-band imaging. To measure medium-band colors, we use the forced photometry for the 7801 sources as outlined in Section 4.2.

We also measure photometric redshifts in our medium-band detected sample (as in Hainline et al. 2023). To enable as accurate as possible redshifts, we make use of a suite of the deepest ancillary optical-near-infrared photometry available in this field, in addition to the new imaging from our medium-band survey (see Section 2.2). We use the redshift at the peak of the photometric redshift distribution measured using EAZY (Brammer et al. 2008). We do not set priors and use the standard EAZY templates with a custom-supplemented set of SED templates that include bluer continuums and stronger line

and nebular continuum emission, which improves photometric redshift recovery for blue, high sSFR galaxies with strong nebular emission (see also Larson et al. 2022). Where spectroscopic redshifts are available, we replace the photometric estimate with the spectroscopic one. We find that, among the Bacon et al. (2023), Kodra et al. (2023), and Oesch et al. (2023) spectroscopic data sets, there are 530 galaxies in our NIRCam medium-band footprint that are spectroscopically confirmed. In general, we find excellent agreement with the photometric redshifts measured using our data, with a $\sigma_{nmad} = 0.013$ and an outlier fraction of only 5.9%. We note that available spectroscopic redshifts are dominated by objects at $z < 2.5$. Restricting our photometric performance to spectroscopic confirmations at $z > 2.5$ where our data sample strong spectral features also demonstrate excellent photometric redshift performance with $\sigma_{nmad} = 0.013$ and an outlier fraction of 5.9%. Thus, we have confidence in the photometric redshift accuracy that we use to plot the redshift evolution of the color distributions plotted in Figure 5.

We find that the simulated color distributions with redshift from JAGUAR are largely reproduced by real galaxies identified in our imaging. In particular, we find that Hα +[N II] and [O III]+Hβ drive the strongest colors at both 2 and 4 μm wavelengths. We also find examples where color excesses are measurable from both Paschen-α (see also Figure 4) and [S III]λ9069, 9532+He I λ10830, in particular, at 4 μm. Of those three lines, the prominent flux excesses in the yellow shaded region in the bottom panel of Figure 5 originate from the He I λ10830 line.

Taking these redshifts and colors at face value, we find that our survey likely identified 66 Hα+[N II] emitters in our 2 μm imaging at $z \sim 1.5$–2.5 with EW > 500 Å (corresponding roughly to absolute color difference >1 mag). At $z \sim 5.5$–6.6, we identified 90 likely Hα+[N II] emitters with EW > 500A in our 4 μm imaging. These numbers are for detections with S/N in the emission-line band of at least 7 (to allow for nondetected continuum; in cases of nondetection, the measured colors are lower limits). Similarly, we identify 217 [O III]+Hβ emitters in our 2 μm imaging at $2.4 < z < 3.5$ and 22 in the 4 μm imaging at $7.3 < z < 9.3$. We note that the NIRISS footprint increases the sample sizes of line emitters at 4.3 and 4.8 μm by $\sim$50%.

In Table 2, we compare our observed number of Hα+[N II] and [O III]+Hβ emitters across redshifts to those predicted by the JAGUAR phenomenological galaxy evolution model. For this comparison, we include JAGUAR sources whose fluxes are S/N > 7 in the emission line as is done for the observed galaxies in Figure 5 while also requiring the continuum band have sensitivity to recover color difference >1 mag (to allow for continuum nondetections). We find that JAGUAR generally underpredicts the number of galaxies with observed medium-band colors >1 mag for the redshift ranges where these emission lines enter our filters (see Table 2). This is in line with recent comparisons finding JAGUAR generally underpredicts strong Hα+[N II] and [O III]+Hβ emitters (De Barros et al. 2019; Maseda et al. 2019; Sun et al. 2023). Possible explanations for the stronger observed lines include more stochastic star formation in real galaxies, poor representation of the tails of real galaxy property distributions that drive strong lines (e.g., log U, the effective gas ionization parameter), and that more extreme stellar populations are not represented in JAGUAR.

Table 2
Estimated Number of Galaxies with Robustly Measured Spectral Features
(Figure 6, Left Panel) in Our NIRCam Pointing

Filter	Feature	Redshift	Predicted N_{obj}[a]	Observed N_{obj}[b]
F182M+F210M	Hα+[N II]	1.5–2.5	35 ± 2	66
	[O III]+Hβ	2.4–3.5	78 ± 3	217
F430M+F460M +F480M	Hα+[N II]	5.3–6.6	63 ± 2	90
	[O III]+Hβ	7.3–9.3	20 ± 1	22

Notes.
[a] Predicted number of sources in our ~10 arcmin^2 NIRCam coverage with JAGUAR above S/N > 7 in the emission-line band. For Hα+[N II] and [O III]+Hb, we show sources with medium-band colors >1 mag (roughly corresponding to EW > 500 Å; see description in Section 5.2).
[b] Observed galaxies in our survey that meet the criteria listed in (a) for each set of emission lines.

5.3. Simulating Emission-line Constraints Using Medium-band Imaging

In this section, we translate our photometric limits into emission-line equivalent width limits to understand the swath of the galaxy population for which we can constrain physical parameters. To make these translations, we make use of the NIRCam photometry and emission-line properties of JAGUAR mock galaxies. In Figure 6, we show the color excesses of JAGUAR galaxies where Hα+[N II] enters the F430M band ($5.3 < z < 5.7$) using one realization of JAGUAR (11×11 arcmin^2). To measure the continuum magnitude near the emission line, we also require significant flux detections in the continuum bands with S/N > 7, and use a linear fit with the F460M and F480M fluxes. The full mock galaxy distribution is shown in black points, while mock galaxies that would be detected at >3σ in our imaging are shown as colors (color coded by their intrinsic equivalent width of Hα emission). It is clear that, as Hα EW increases, so do the observed 4 μm color excesses. The galaxies with observed colors that are in excess of the red dashed line have Hα EWs that are measurable using colors at the >3σ level by our survey (e.g., Bunker et al. 1995; Shioya et al. 2009; Sobral et al. 2013). Scaled to the JEMS survey area, JAGUAR predicts 30 ± 2 Hα emitters with measured color significance >3σ, although, as noted in Section 5.2, the real survey contains more candidate emitters above this significance, since the galaxies in our survey demonstrate stronger Hα emission lines. We find that we are sensitive to rest-frame Hα EW $\gtrsim 50$ Å at brighter magnitudes (<24–26 AB), and near our detection limit, we can still identify sources with rest-frame EW $\gtrsim 2500$ Å.

In the right panel of Figure 6, we plot the SFR versus $M_\star$ for mock galaxies with EWs that can be measured as detectable color excesses at the >3σ level (colored points). The right panel contains objects identified using the analogous selection for emission lines inside both F460M and F480M, in addition to F430M (which is presented as an example in the left plot). In this right panel, we convert the intrinsic Hα luminosity (as observed, uncorrected for dust attenuation) of the detectable mock galaxies to an unobscured SFR(Hα) using Kennicutt (1998), converted to Chabrier (2003) initial mass function. We find that, given our deep imaging limits, the galaxies for which we are able to robustly measure color excesses from Hα

include the galaxies with SFR as low as $\gtrsim 0.7\,M_\odot\,\mathrm{yr}^{-1}$ (right panel of Figure 6).

Given our imaging detection limits, this includes the galaxies with line fluxes as low as $\log F > -18$ erg s^{-1} cm^{-2} (but note that our sensitivity to line flux depends on apparent magnitude and is not a uniform limit). Compared to existing JWST grism observations (FRESCO with 5σ line flux sensitivity $\gtrsim 2 \times 10^{-18}$ erg s^{-1} cm^{-2} between 4.3 and 4.6 μm; Oesch et al. 2023), we find our imaging is roughly 2$\times$ deeper at 4 μm in terms of emission-line flux sensitivity (for EW with detectable colors).

This demonstrates our medium-band imaging can provide emission-line and related physical parameter constraints for galaxies in new parameter space from across redshifts from $0.3 < z \lesssim 20$. Figure 6 shows the power of our data set to constrain uncertain parameters such as SFR and emission-line strength. This result is in line with the analysis presented elsewhere demonstrating quantitatively that JWST medium-band imaging improves physical parameter recovery in high-redshift galaxies (Roberts-Borsani et al. 2021).

6. Plans for Release of Higher-level Data Products

With this paper, we make publicly available our first data release that includes version 1 of our science-ready mosaics, enabling the community to begin exploiting this exciting data set. In the future, we plan additional data product releases, including science-ready photometric catalogs with value-added parameters. Additionally, these data are integrated into the JADES survey data products (Eisenstein et al. 2023; Rieke & the JADES Collaboration 2023), including mosaics that are astrometrically aligned with and photometric catalogs incorporating existing HST data.

7. Summary

We have planned and executed JEMS, a five-filter medium-band survey with JWST in Cycles 1 at 2 and 4 μm wavelength. Our survey includes F182M, F210M, F430M, F460M, and F480M images taken with NIRCam over the HUDF and coordinated parallel NIRISS images using F430M and F480M that fall on the CANDELS footprint in GOODS-S. The reduced JWST data[25] produced by this program are available as a high-level science product via MAST at doi:10.17909/fsc4-dt61. In this work, we have demonstrated that our data are capable of measuring and characterizing strong emission lines at all redshifts from $0.3 < z \lesssim 20$, opening the door to better constrained physical parameters in high-redshift galaxies. The medium-band imaging with JWST represents a new and exciting resource with high efficiency compared to spectroscopy, enabling new science across redshifts as demonstrated in this paper.

---

[25] https://archive.stsci.edu/hlsp/jems

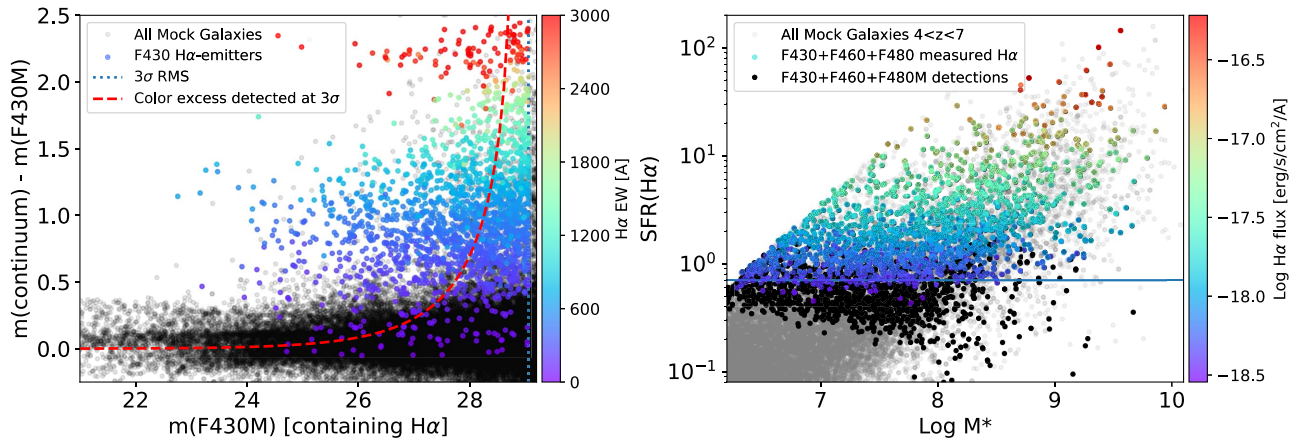**Figure 6.** Left panel: mock observations using JAGUAR simulating our 4 μm selected Hα source population (colored points) from their color excess in our medium bands. (example shown is for $5.3 < z < 5.7$ using Hα emitters identified from F430M excess in one realization of JAGUAR; 120 arcmin^2). Continuum is measured using the other medium bands (F460M, F480M). Rainbow points in excess of the red line have robustly measured color excesses ($>3\sigma$; e.g., Bunker et al. 1995). Right panel: region of the SFR–M_* diagram where our survey can robustly measure Hα from color excesses in all three 4 μm filters (using criteria demonstrated in the left panel), which roughly corresponds to a limiting unobscured SFR traced by Hα of ∼0.7 $M_\odot$ yr^{-1} where equivalent width is measurable (indicated by a horizontal line; number counts in Table 2).

Appendix

To facilitate joint analysis of our new JWST imaging with existing HST imaging (e.g., HLF, Whitaker et al. 2019), we document here the astrometric adjustments that we performed to public mosaics available elsewhere. As described in Section 3, the astrometry of our mosaics is tied to the Gaia system. Therefore, one can coanalyze with the CHArGE imaging (although we note that their 100 mas pixel scale is different from ours, which are 30 mas pixels).

Alternatively, one can use the HLF imaging (v2.0) with the same 30 mas pixel scale (and the same nominal pixel registration) if the HLF image header information is updated. We provide these updates here, which involve both a reference pixel offset and a slight rescaling of pixel size. To adjust the pixel offset, we update the CRVAL1 and CRVAL2 values by −4.08 and +2.76 mas respectively. To rescale the pixel size, we scale the CD1_1 and CD2_2 values by 0.9998258, 0.9998248 respectively. We will provide a Python script on our data release page that will perform these adjustments to the HLF images and catalog coordinates.

ORCID iDs

Christina C. Williams ⓘ https://orcid.org/0000-0003-2919-7495
Sandro Tacchella ⓘ https://orcid.org/0000-0002-8224-4505
Michael V. Maseda ⓘ https://orcid.org/0000-0003-0695-4414
Brant E. Robertson ⓘ https://orcid.org/0000-0002-4271-0364
Benjamin D. Johnson ⓘ https://orcid.org/0000-0002-9280-7594
Chris J. Willott ⓘ https://orcid.org/0000-0002-4201-7367
Daniel J. Eisenstein ⓘ https://orcid.org/0000-0002-2929-3121

Christopher N. A. Willmer ⬡ https://orcid.org/0000-0001-9262-9997

Zhiyuan Ji ⬡ https://orcid.org/0000-0001-7673-2257

Kevin N. Hainline ⬡ https://orcid.org/0000-0003-4565-8239

Jakob M. Helton ⬡ https://orcid.org/0000-0003-4337-6211

Stacey Alberts ⬡ https://orcid.org/0000-0002-8909-8782

Rachana Bhatawdekar ⬡ https://orcid.org/0000-0003-0883-2226

Kristan Boyett ⬡ https://orcid.org/0000-0003-4109-304X

Stefano Carniani ⬡ https://orcid.org/0000-0002-6719-380X

Stephane Charlot ⬡ https://orcid.org/0000-0003-3458-2275

Jacopo Chevallard ⬡ https://orcid.org/0000-0002-7636-0534

Emma Curtis-Lake ⬡ https://orcid.org/0000-0002-9551-0534

Anna de Graaff ⬡ https://orcid.org/0000-0002-2380-9801

Eiichi Egami ⬡ https://orcid.org/0000-0003-1344-9475

Marijn Franx ⬡ https://orcid.org/0000-0002-8871-3026

Nimisha Kumari ⬡ https://orcid.org/0000-0002-5320-2568

Roberto Maiolino ⬡ https://orcid.org/0000-0002-4985-3819

Erica J. Nelson ⬡ https://orcid.org/0000-0002-7524-374X

Marcia J. Rieke ⬡ https://orcid.org/0000-0002-7893-6170

Lester Sandles ⬡ https://orcid.org/0000-0001-9276-7062

Irene Shivaei ⬡ https://orcid.org/0000-0003-4702-7561

Charlotte Simmonds ⬡ https://orcid.org/0000-0003-4770-7516

Renske Smit ⬡ https://orcid.org/0000-0001-8034-7802

Katherine A. Suess ⬡ https://orcid.org/0000-0002-1714-1905

Fengwu Sun ⬡ https://orcid.org/0000-0002-4622-6617

Hannah Übler ⬡ https://orcid.org/0000-0003-4891-0794

Joris Witstok ⬡ https://orcid.org/0000-0002-7595-121X

References

Adams, N. J., Conselice, C. J., Ferreira, L., et al. 2023, MNRAS, 518, 4755
Akhshik, M., Whitaker, K. E., Brammer, G., et al. 2020, ApJ, 900, 184
Akhshik, M., Whitaker, K. E., Leja, J., et al. 2023, ApJ, 943, 179
Astropy Collaboration, Price-Whelan, A. M., Lim, P. L., et al. 2022, ApJ, 935, 167
Astropy Collaboration, Robitaille, T. P., Tollerud, E. J., et al. 2013, A&A, 558, A33
Atek, H., Chemerynska, I., Wang, B., et al. 2023a, MNRAS, 524, 5486
Atek, H., Richard, J., Jauzac, M., et al. 2015, ApJ, 814, 69
Atek, H., Shuntov, M., Furtak, L. J., et al. 2023b, MNRAS, 519, 1201
Bacon, R., Brinchmann, J., Conseil, S., et al. 2023, A&A, 670, A4
Bagley, M. B., Finkelstein, S. L., Koekemoer, A. M., et al. 2023a, ApJL, 946, L12
Bagley, M. B., Pirzkal, N., Finkelstein, S. L., et al. 2023b, arXiv:2302.05466
Barrow, K. S. S., Robertson, B. E., Ellis, R. S., et al. 2020, ApJL, 902, L39
Beckwith, S. V. W., Stiavelli, M., Koekemoer, A. M., et al. 2006, AJ, 132, 1729
Bertin, E., & Arnouts, S. 1996, A&AS, 117, 393
Bezanson, R., Labbe, I., Whitaker, K. E., et al. 2022, arXiv:2212.04026
Bonoli, S., Marín-Franch, A., Varela, J., et al. 2021, A&A, 653, A31
Bouwens, R. J., Illingworth, G. D., Oesch, P. A., et al. 2015, ApJ, 811, 140
Bouwens, R. J., Stefanon, M., Brammer, G., et al. 2023, MNRAS, 523, 1036
Bowler, R. A. A., Bourne, N., Dunlop, J. S., McLure, R. J., & McLeod, D. J. 2018, MNRAS, 481, 1631
Bowler, R. A. A., Cullen, F., McLure, R. J., Dunlop, J. S., & Avison, A. 2022, MNRAS, 510, 5088
Boyer, M. L., Anderson, J., Gennaro, M., et al. 2022, RNAAS, 6, 191
Boyett, K. N. K., Stark, D. P., Bunker, A. J., Tang, M., & Maseda, M. V. 2022, MNRAS, 513, 4451
Bradač, M. 2020, NatAs, 4, 478
Bradley, L., Sipőcz, B., Robitaille, T., et al. 2022, astropy/photutils: 1.5.0, v1.5.0, Zenodo, doi:10.5281/zenodo.6825092
Bradley, L. D., Coe, D., Brammer, G., et al. 2023, ApJ, 955, 13
Brammer, G. B., Sánchez-Janssen, R., Labbé, I., et al. 2012, ApJL, 758, L17
Brammer, G. B., van Dokkum, P. G., & Coppi, P. 2008, ApJ, 686, 1503
Bunker, A. J., Stanway, E. R., Ellis, R. S., & McMahon, R. G. 2004, MNRAS, 355, 374

Bunker, A. J., Warren, S. J., Hewett, P. C., & Clements, D. L. 1995, MNRAS, 273, 513
Bunker, A. J., Wilkins, S., Ellis, R. S., et al. 2010, MNRAS, 409, 855
Calabrò, A., Daddi, E., Cassata, P., et al. 2018, ApJL, 862, L22
Cardamone, C. N., van Dokkum, P. G., Urry, C. M., et al. 2010, ApJS, 189, 270
Casey, C. M., Zavala, J. A., Aravena, M., et al. 2019, ApJ, 887, 55
Chabrier, G. 2003, PASP, 115, 763
Chevallard, J., & Charlot, S. 2016, MNRAS, 462, 1415
Chevallard, J., Curtis-Lake, E., Charlot, S., et al. 2019, MNRAS, 483, 2621
Cleri, N. J., Trump, J. R., Backhaus, B. E., et al. 2022, ApJ, 929, 3
Colbert, J. W., Teplitz, H., Atek, H., et al. 2013, ApJ, 779, 34
Curtis-Lake, E., Carniani, S., Cameron, A., et al. 2023, NatAs, 7, 622
Curtis-Lake, E., Chevallard, J., Charlot, S., & Sandles, L. 2021, MNRAS, 503, 4855
De Barros, S., Oesch, P. A., Labbé, I., et al. 2019, MNRAS, 489, 2355
de Barros, S., Schaerer, D., & Stark, D. P. 2014, A&A, 563, A81
Donnan, C. T., McLeod, D. J., Dunlop, J. S., et al. 2023a, MNRAS, 518, 6011
Donnan, C. T., McLeod, D. J., McLure, R. J., et al. 2023b, MNRAS, 520, 4554
Doyon, R., Hutchings, J. B., Beaulieu, M., et al. 2012, Proc. SPIE, 8442, 84422R
Doyon, R., Willott, C. J., Hutchings, J. B., et al. 2023, PASP, 135, 098001
Dunlop, J. S., Abraham, R. G., Ashby, M. L. N., et al. 2021, PRIMER: Public Release IMaging for Extragalactic Research, JWST Proposal, 1837
Eisenstein, D. J., Willott, C., Alberts, S., et al. 2023, arXiv:2306.02465
Endsley, R., Stark, D. P., Chevallard, J., & Charlot, S. 2021, MNRAS, 500, 5229
Endsley, R., Stark, D. P., Whitler, L., et al. 2023, MNRAS, 524, 2312
Esdaile, J., Labbé, I., Glazebrook, K., et al. 2021, AJ, 162, 225
Eyles, L. P., Bunker, A. J., Ellis, R. S., et al. 2007, MNRAS, 374, 910
Eyles, L. P., Bunker, A. J., Stanway, E. R., et al. 2005, MNRAS, 364, 443
Faisst, A. L., Capak, P., Hsieh, B. C., et al. 2016, ApJ, 821, 122
Faisst, A. L., Capak, P. L., Emami, N., Tacchella, S., & Larson, K. L. 2019, ApJ, 884, 133
Ferland, G. J., Porter, R. L., van Hoof, P. A. M., et al. 2013, RMxAA, 49, 137
Ferruit, P., Jakobsen, P., Giardino, G., et al. 2022, A&A, 661, A81
Finkelstein, S. L., Bagley, M. B., Ferguson, H. C., et al. 2023, ApJL, 946, L13
Finkelstein, S. L., D'Aloisio, A., Paardekooper, J.-P., et al. 2019, ApJ, 879, 36
Finkelstein, S. L., Ryan, R. E. J., Papovich, C., et al. 2015, ApJ, 810, 71
Fletcher, T. J., Tang, M., Robertson, B. E., et al. 2019, ApJ, 878, 87
Forrest, B., Marsan, Z. C., Annunziatella, M., et al. 2020, ApJ, 903, 47
Förster Schreiber, N. M., Renzini, A., Mancini, C., et al. 2018, ApJS, 238, 21
Fruchter, A. S., & Hook, R. N. 2002, PASP, 114, 144
Gaia Collaboration, Brown, A. G. A., Vallenari, A., et al. 2016, A&A, 595, A2
Gaia Collaboration, Brown, A. G. A., Vallenari, A., et al. 2018, A&A, 616, A1
Gardner, J. P., Mather, J. C., Abbott, R., et al. 2023, PASP, 135, 068001
Giavalisco, M., Ferguson, H. C., Koekemoer, A. M., et al. 2004, ApJL, 600, L93
Giménez-Arteaga, C., Brammer, G. B., Marchesini, D., et al. 2022, ApJS, 263, 17
Glazebrook, K., Schreiber, C., Labbé, I., et al. 2017, Natur, 544, 71
Gordon, K. D., Bohlin, R., Sloan, G. C., et al. 2022, AJ, 163, 267
Grogin, N. A., Kocevski, D. D., Faber, S. M., et al. 2011, ApJS, 197, 35
Hainline, K. N., Johnson, B. D., Robertson, B., et al. 2023, arXiv:2306.02468
Harikane, Y., Ouchi, M., Oguri, M., et al. 2023, ApJS, 265, 5
Hatsukade, B., Kohno, K., Yamaguchi, Y., et al. 2018, PASJ, 70, 105
Illingworth, G., Magee, D., Bouwens, R., et al. 2016, arXiv:1606.00841
Inoue, A. K., Shimizu, I., Iwata, I., & Tanaka, M. 2014, MNRAS, 442, 1805
Ji, Z., Williams, C. C., Tacchella, S., et al. 2023, arXiv:2305.18518
Katz, H., Saxena, A., Cameron, A. J., et al. 2023, MNRAS, 518, 592
Kauffmann, O. B., Le Fèvre, O., Ilbert, O., et al. 2020, A&A, 640, A67
Keating, L. C., Weinberger, L. H., Kulkarni, G., et al. 2020, MNRAS, 491, 1736
Kemp, T. W., Dunlop, J. S., McLure, R. J., et al. 2019, MNRAS, 486, 3087
Kennicutt, R. C., & Evans, N. J. 2012, ARA&A, 50, 531
Kennicutt, R. C., Jr. 1998, ApJ, 498, 541
Kodra, D., Andrews, B. H., Newman, J. A., et al. 2023, ApJ, 942, 36
Labbé, I., Oesch, P. A., Bouwens, R. J., et al. 2013, ApJL, 777, L19
Labbe, I., van Dokkum, P., Nelson, E., et al. 2023, Natur, 616, 266
Lam, D., Bouwens, R. J., Labbé, I., et al. 2019, A&A, 627, A164
Laporte, N., Ellis, R. S., Witten, C. E. C., & Roberts-Borsani, G. 2023, MNRAS, 523, 3018
Larson, R. L., Hutchison, T. A., Bagley, M., et al. 2022, arXiv:2211.10035
Long, A. S., Casey, C. M., Lagos, C. d. P., et al. 2023, ApJ, 953, 11
Lorenzoni, S., Bunker, A. J., Wilkins, S. M., et al. 2013, MNRAS, 429, 150
Madau, P., & Dickinson, M. 2014, ARA&A, 52, 415
Manning, S. M., Casey, C. M., Zavala, J. A., et al. 2022, ApJ, 925, 23
Marchesini, D., Brammer, G., Morishita, T., et al. 2023, ApJL, 942, L25

Marrone, D. P., Spilker, J. S., Hayward, C. C., et al. 2018, Natur, 553, 51
Maseda, M. V., Bacon, R., Lam, D., et al. 2020, MNRAS, 493, 5120
Maseda, M. V., Franx, M., Chevallard, J., & Curtis-Lake, E. 2019, MNRAS, 486, 3290
Matharu, J., Muzzin, A., Brammer, G. B., et al. 2021, ApJ, 923, 222
Matthee, J., Naidu, R. P., Pezzulli, G., et al. 2022, MNRAS, 512, 5960
McGreer, I. D., Mesinger, A., & D'Odorico, V. 2015, MNRAS, 447, 499
Mingozzi, M., Belfiore, F., Cresci, G., et al. 2020, A&A, 636, A42
Moles, M., Benítez, N., Aguerri, J. A. L., et al. 2008, AJ, 136, 1325
Momcheva, I. G., Brammer, G. B., van Dokkum, P. G., et al. 2016, ApJS, 225, 27
Naidu, R. P., Oesch, P. A., van Dokkum, P., et al. 2022, ApJL, 940, L14
Naidu, R. P., Tacchella, S., Mason, C. A., et al. 2020, ApJ, 892, 109
Nakajima, K., Ellis, R. S., Iwata, I., et al. 2016, ApJL, 831, L9
Nanayakkara, T., Glazebrook, K., Jacobs, C., et al. 2022, arXiv:2212.11638
Nelson, E. J., Tacchella, S., Diemer, B., et al. 2021, MNRAS, 508, 219
Nelson, E. J., van Dokkum, P. G., Förster Schreiber, N. M., et al. 2016, ApJ, 828, 27
Ning, Y., Cai, Z., Jiang, L., et al. 2023, ApJ, 944, L1
Oesch, P. A., Brammer, G., Naidu, R. P., et al. 2023, MNRAS, 525, 2864
Papovich, C., Rudnick, G., Rigby, J. R., et al. 2009, ApJ, 704, 1506
Pasha, I., Leja, J., van Dokkum, P. G., Conroy, C., & Johnson, B. D. 2020, ApJ, 898, 165
Pérez-González, P. G., Cava, A., Barro, G., et al. 2013, ApJ, 762, 46
Perrin, M. D., Long, J., Sivaramakrishnan, A., et al. 2015, WebbPSF: James Webb Space Telescope PSF Simulation Tool, Astrophysics Source Code Library, ascl:1504.007
Perrin, M. D., Sivaramakrishnan, A., Lajoie, C.-P., et al. 2014, Proc. SPIE, 9143, 91433X
Planck Collaboration, Aghanim, N., Akrami, Y., et al. 2020, A&A, 641, A6
Rasappu, N., Smit, R., Labbé, I., et al. 2016, MNRAS, 461, 3886
Rieke, M. & the JADES Collaboration 2023, arXiv:2306.02466
Rieke, M. J., Kelly, D., & Horner, S. 2005, Proc. SPIE, 5904, 1
Rieke, M. J., Kelly, D. M., Misselt, K., et al. 2023, PASP, 135, 028001
Rigby, J., Perrin, M., McElwain, M., et al. 2023, PASP, 135, 048001
Roberts-Borsani, G., Treu, T., Mason, C., et al. 2021, ApJ, 910, 86
Robertson, B. E. 2022, ARA&A, 60, 121
Robertson, B. E., Furlanetto, S. R., Schneider, E., et al. 2013, ApJ, 768, 71
Robertson, B. E., Tacchella, S., Johnson, B. D., et al. 2023, NatAs, 7, 611
Rujopakarn, W., Rieke, G. H., Papovich, C. J., et al. 2012, ApJ, 755, 168
Rujopakarn, W., Williams, C. C., Daddi, E., et al. 2023, ApJL, 948, L8
Santini, P., Castellano, M., Fontana, A., et al. 2022, ApJ, 940, 135
Schreiber, C., Glazebrook, K., Nanayakkara, T., et al. 2018, A&A, 618, A85

Scoville, N., Aussel, H., Brusa, M., et al. 2007, ApJS, 172, 1
Shim, H., Chary, R.-R., Dickinson, M., et al. 2011, ApJ, 738, 69
Shioya, Y., Taniguchi, Y., Sasaki, S. S., et al. 2009, ApJ, 696, 546
Simmonds, C., Tacchella, S., Maseda, M., et al. 2023, MNRAS, 523, 5468
Skelton, R. E., Whitaker, K. E., Momcheva, I. G., et al. 2014, ApJS, 214, 24
Smit, R., Bouwens, R. J., Franx, M., et al. 2015, ApJ, 801, 122
Smit, R., Bouwens, R. J., Labbé, I., et al. 2014, ApJ, 784, 58
Smit, R., Bouwens, R. J., Labbé, I., et al. 2016, ApJ, 833, 254
Sobral, D., Smail, I., Best, P. N., et al. 2013, MNRAS, 428, 1128
Stark, D. P. 2016, ARA&A, 54, 761
Stark, D. P., Schenker, M. A., Ellis, R., et al. 2013, ApJ, 763, 129
Stefanon, M., Bouwens, R. J., Illingworth, G. D., et al. 2022, ApJ, 935, 94
Straatman, C. M. S., Spitler, L. R., Quadri, R. F., et al. 2016, ApJ, 830, 51
Strom, A. L., Steidel, C. C., Rudie, G. C., et al. 2017, ApJ, 836, 164
Sun, F., Egami, E., Pérez-González, P. G., et al. 2021, ApJ, 922, 114
Sun, F., Egami, E., Pirzkal, N., et al. 2023, ApJ, 953, 53
Tacchella, S., Carollo, C. M., Renzini, A., et al. 2015, Sci, 348, 314
Tacchella, S., Dekel, A., Carollo, C. M., et al. 2016, MNRAS, 458, 242
Tacchella, S., Finkelstein, S. L., Bagley, M., et al. 2022, ApJ, 927, 170
Tacchella, S., Johnson, B. D., Robertson, B. E., et al. 2023, MNRAS, 522, 6236
Tang, M., Stark, D. P., Chevallard, J., et al. 2021, MNRAS, 503, 4105
Valentino, F., Tanaka, M., Davidzon, I., et al. 2020, ApJ, 889, 93
van Dokkum, P. G., Labbé, I., Marchesini, D., et al. 2009, PASP, 121, 2
Wang, T., Schreiber, C., Elbaz, D., et al. 2019, Natur, 572, 211
Wellons, S., Torrey, P., Ma, C.-P., et al. 2015, MNRAS, 449, 361
Whitaker, K. E., Ashas, M., Illingworth, G., et al. 2019, ApJS, 244, 16
Whitaker, K. E., Labbé, I., van Dokkum, P. G., et al. 2011, ApJ, 735, 86
Whitler, L., Endsley, R., Stark, D. P., et al. 2023, MNRAS, 519, 157
Wilkins, S. M., Bunker, A. J., Stanway, E., Lorenzoni, S., & Caruana, J. 2011, MNRAS, 417, 717
Wilkins, S. M., Vijayan, A. P., Lovell, C. C., et al. 2022, MNRAS, 517, 3227
Williams, C. C., Curtis-Lake, E., Hainline, K. N., et al. 2018, ApJS, 236, 33
Williams, C. C., Labbe, I., Spilker, J., et al. 2019, ApJ, 884, 154
Williams, C. C., Oesch, P., Barrufet, L., et al. 2021, PANORAMIC—A Pure Parallel Wide Area Legacy Imaging Survey at 1-5 Micron, JWST Proposal, 2514
Willott, C. J., Doyon, R., Albert, L., et al. 2022, PASP, 134, 025002
Windhorst, R. A., Cohen, S. H., Jansen, R. A., et al. 2023, AJ, 165, 13
Wisotzki, L., Bacon, R., Brinchmann, J., et al. 2018, Natur, 562, 229
Wolf, C., Meisenheimer, K., Kleinheinrich, M., et al. 2004, A&A, 421, 913